RESEARCH ARTICLE

National Science Open
2: 20220058, 2023
https://doi.org/10.1360/nso/20220058

Materials Science

Special Topic: Glasses—Materials and Physics

Generalization of the Hall-Petch and inverse Hall-Petch behaviors by tuning amorphous regions in 2D solids

Zhibin Xu[1,2], Mengmeng Li[3], Huijun Zhang[4,*] & Yilong Han[1,5,*]

[1]*Department of Physics, The Hong Kong University of Science and Technology, Hong Kong 999077, China;*
[2]*Function Hub, The Hong Kong University of Science and Technology (Guangzhou), Guangzhou 510000, China;*
[3]*Department of Mechanical & Aerospace Engineering, The Hong Kong University of Science and Technology, Hong Kong 999077, China;*
[4]*State Key Laboratory for Mechanical Behavior of Materials, Shaanxi International Research Center for Soft Matter, School of Materials Science and Engineering, Xi'an Jiaotong University, Xi'an 710049, China;*
[5]*The Hong Kong University of Science and Technology Shenzhen Research Institute, Shenzhen 518057, China*

*Corresponding authors (emails: huijun@xjtu.edu.cn (Huijun Zhang); yilong@ust.hk (Yilong Han))

Received 1 September 2022; Revised 24 October 2022; Accepted 5 December 2022; Published online 20 April 2023

Abstract: The strength $\sigma_y(D)$ of a polycrystal can decrease or increase with the grain diameter D, i.e., the famous Hall-Petch (HP) and inverse-Hall-Petch (IHP) behaviors, respectively. However, $\sigma_y(D)$ under thick grain boundaries (GBs) (i.e., GB thickness $l > 1$ particle) and $\sigma_y(l)$ have rarely been explored. Here we measure them by systematically varying D and l of two-dimensional glass-crystal composites in simulations. We demonstrate that increasing l and decreasing D have similar effects on reducing dislocation motions and promoting GB deformations. Consequently, the classical HP-IHP behaviors of $\sigma_y(D, l = 1)$ and our generalized HP-IHP behaviors of $\sigma_y(D, l)$ share similar mechanisms and can be unified as σ_y (A_{GB}/A_{tot}), where A_{GB}/A_{tot} is the fraction of the amorphous region. The results reveal a way to exceed the maximum strength of normal polycrystals. The generalized HP-IHP behaviors of $\sigma_y(D, l)$ should be similar in 2D and 3D, except that the HP effect in 3D is stronger.

Keywords: polycrystal, amorphous solid, crystal-glass crossover, Hall-Petch strengthening, inverse Hall-Petch weakening

INTRODUCTION

Crystalline and amorphous materials are ubiquitous in nature and are widely used in the industry [1]. However, their crossover regime is much less explored and poorly understood [2]. Conventional crystals, such as silicon [3] or water ice [4] crystal can be catastrophically compressed into an amorphous solid (i.e., a glass) without forming intermediate structures of crystalline and amorphous mixtures. In recent years, glass-crystal composites (GCCs), also known as dual-phase materials, have been fabricated especially for amorphous-nanocrystalline alloys [5]. They possess the advantages of both crystals and glasses and exhibit exceptional properties, such as ultrahigh strength [6], super plasticity [7, 8], high reversible strain, world-record fatigue life [9], and less strength-ductility tradeoff [2, 10], thus resulting in their broad industrial applications. These super alloys are typically fabricated by severe plastic deformation [11, 12], whose microscopic kinetics are unclear. The size and shape of crystalline and amorphous regions can hardly be controlled; thus, their effect

on material properties has been poorly explored and understood. Furthermore, while great efforts have been made to improve GCC's properties, their trial-and-error fabrication processes have limited theoretical rationale. Simulations show that thick amorphous regions better absorb dislocation [8] and suppress dislocation formation [13], but studies about the impact of l on material properties are very limited [8, 14–16].

The effect of mean grain diameter D has been well-studied in polycrystals, such as ceramics, metals and alloys with normal thin GB (i.e., $l \simeq 1$ particle) [17]. The strength, or yield stress σ_y, increases as D decreases, i.e., the famous Hall-Petch (HP) behavior [18, 19] discovered in 1950s. This trend reverses in $3 \lesssim D \lesssim 10$–15 nm, i.e., the inverse Hall-Petch (IHP) behavior [20–22]. The HP and IHP behaviors generally hold in atomic and molecular polycrystals. However, when the GB thickness l is not as thin as about one particle in traditional polycrystals, how does D affect material properties? Moreover, how does σ_y vary with the GB thickness l and does it exhibit HP- and IHP-like behaviors? These questions have rarely been investigated. Recent simulations found that σ_y of Cu-based GCCs is higher at $l = 1.0$ nm than those at $l = 0.5$ and 1.5 nm [14, 15], suggesting a nontrivial $\sigma_y(l)$. Similar behavior has also been reported by a simulation of quasi-two-dimensional high entropy GCC alloys, which focuses on the deformation mechanism of thick GB materials [16].

Motivated by the above basic questions, in this study, we measure the strength of solids by systemically changing D and l using two-dimensional (2D) molecular dynamics simulations. The traditional HP and IHP behaviors of $\sigma_y(D, l = 1)$ are generalized to $\sigma_y(D, l)$. The maximum $\sigma_y(D, l)$ exceeds the maximum $\sigma_y(D)$, thus providing a new approach to enhance the strength of solids.

The properties of a GCC can only be properly measured when it contains a sufficient number of crystalline grains, which is computationally expensive for three-dimensional (3D) samples, especially at large D and l. Therefore, we simulate 2D samples that are also poorly explored. 2D materials have attracted great interest in recent years because of their novel properties thanks to the new fabrication techniques. For example, 2D polycrystalline graphene [23,24], silicene [25], 2D amorphous cobalt-anadium hydroxide [26], and vanadium pentoxide [27] show exceptional chemical, physical, electronic, and surface properties [28]. Fabricating 2D solids with thick GBs is challenging. Monodispersed isotropic particles at high densities in 2D only form single crystals or polycrystals without amorphous domains, because the local favorable packing (i.e., equilateral triangle) is compatible with the global favorable packing (i.e., triangular lattice) without geometrical frustrations. Thus, we use binary-sized particles to form the amorphous GB regions and monodispersed particles in the crystalline regions. This should be one of the simplest model systems to achieve GCCs. Such composition distribution is common in polycrystals (e.g., carbon atoms segregating on the GBs of stainless steels) and in GCCs (e.g., binary Cu-Zr [13] or Ni-Co [29] amorphous regions with monodispersed Cu or Ni crystalline regions).

SIMULATION SYSTEM

The molecular dynamics simulations are conducted using large-scale atomic/molecular massively parallel simulator (LAMMPS) [30]. Two particles at separation r have the 12-6 Lennard-Jones potential:

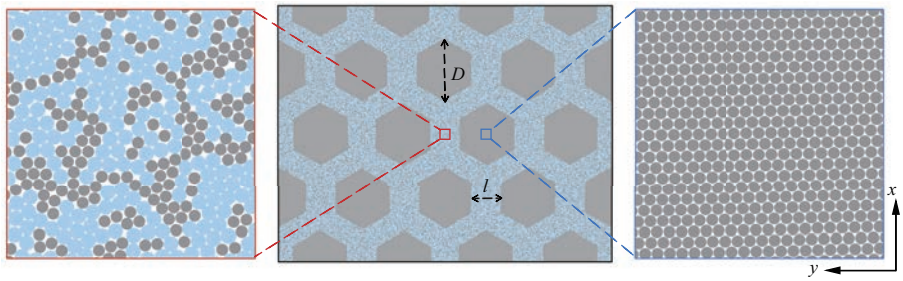

Figure 1 The initial 2D GCC is composed of crystalline grains with diameter $D = 100$ in an amorphous matrix with thickness $l = 40$. The zoom-in of the local amorphous and crystalline areas are shown in the left and right panels, respectively. The amorphous region is a 50%:50% mixture of large (blue) and small (grey) particles. The 16 crystalline grains have random lattice orientations and are composed of small particles.

$$U(r) = 4U_0\left[\left(\frac{d}{r}\right)^{12} - \left(\frac{d}{r}\right)^{6}\right], \quad \text{at } r < r_c. \tag{1}$$

$U(r > r_c) = 0$, where the cutoff $r_c = 2.5d$. $U(r)$ is shifted to 0 at r_c. The diameters d of small and large particles are 1 and 1.3, respectively. Such size ratio has high glass-forming ability and has been widely used in 2D glass studies [31]. We set $(d, U_0) = (1.0, 3), (1.15, 2)$, and $(1.3, 1)$ for interactions between small-small, small-large and large-large particles, respectively, because smaller particles with short separations are often set to have a stronger interaction against phase separation [32].

Bidispersed particles are packed into amorphous GBs with thickness l, and monodispersed small particles are packed into hexagonal lattice domains with diameter D (Figure 1). The sample contains 16 crystalline grains with the periodic boundary conditions. The number of particles ranges from 5000 to 1.4 million in samples with small and large (l, D). To prepare a sample, we first produce a glass by rapidly quenching a liquid composed of 50%:50% binary spheres to temperature $T = 0.2T^*$ during 5τ time period and well relax it for 200τ so that the structure does not change over time. Then the 16 hexagonal regions are replaced by single crystalline grains composed of monodispersed particles. The lattice orientation difference between adjacent grains is randomly set in the range of 10° to 15°. Such sample is relaxed in the NPT ensemble at $0.5T^*$ and hydrostatic pressure $40P^*$ for 200τ, and then changed to $0.2T^*$ at $40P^*$ during 200τ and further equilibrates for 200τ before the measurement. The units $P^* = U_0/d^2$, $\tau = \sqrt{md^2/U_0}$ and $T^* = U_0/k_B$ where the Boltzmann constant $k_B = 1$. All particles have the unit mass $m = 1$.

STRENGTH σ_y AS A FUNCTION OF D AND l

A uniaxial compression is applied along the x direction (Figure 1), deforming the sample with a compression strain ε. The yield stress and flow stress are very close and usually regarded as the same as the virial stress in simulations [33, 34]. The measured stress-strain curves at different l in Figures 2A and S1 (Supporting Information) all exhibit the standard shape with three regimes: a linear increase (i.e., elastic regime), a nonlinear increase (i.e., strain-hardening), and a plateau (i.e., steady flow). The sawtooth shape of the plateau reflects the short quasi-elastic events, such as dislocation nucleation and movement in small systems [35]. We measure the mean flow stress by the plateau height at $7.5\% < \varepsilon < 10\%$ in three trials of simulations as

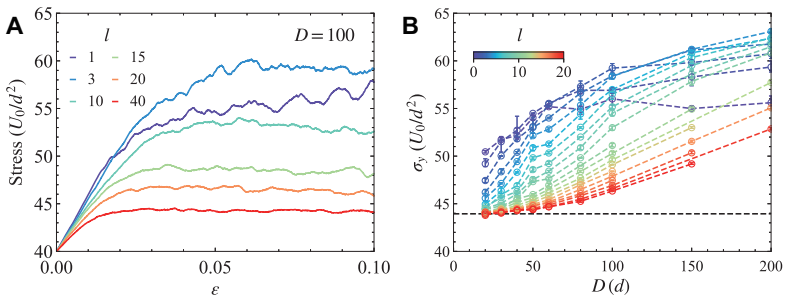

Figure 2 (A) Stress-strain curves of GCCs with $D = 100$. (B) Strength σ_y, i.e., the plateau height in (A), at different grain diameter D and GB thickness l. The horizontal dotted line represents the measured strength of the completely disordered glass.

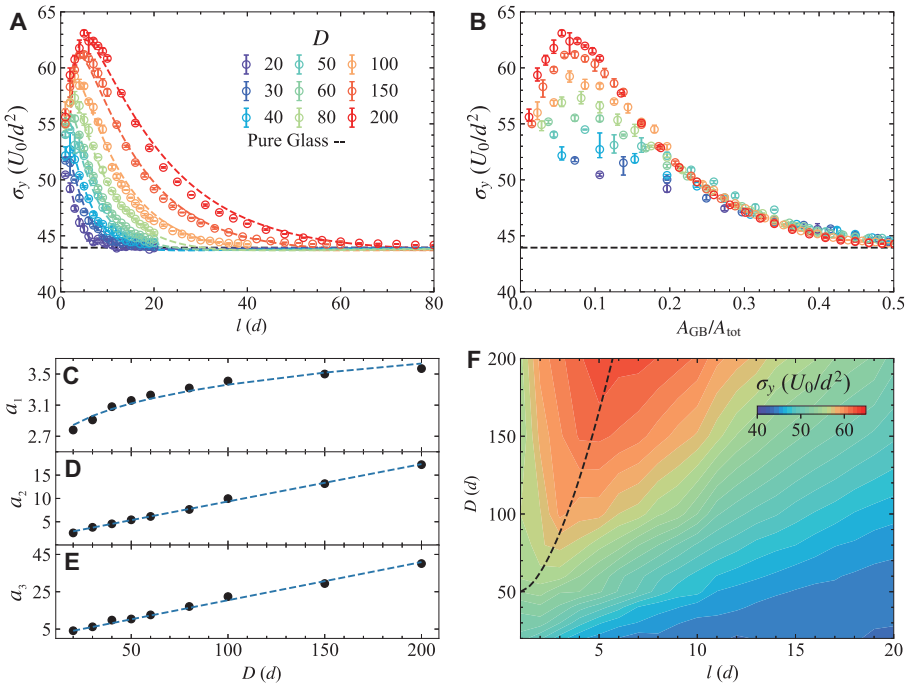

Figure 3 (A) Strength σ_y of GCCs with different grain diameters D and GB thicknesses l fitted with $\sigma_y(D, l) = e^{a_1 - l/a_2} - a_3 l^{-1} + 44$. (B) Replots of (A) by the fraction of GB area A_{GB}/A_{tot}. The horizontal dotted lines in (A) and (B) represent the strength of the completely disordered glass. (C)–(E) The fitting parameters from (A). (C) $a_1 = 0.35\log(D) - 1.76$. (D) $a_2 = 0.08D + 1.34$. (E) $a_3 = 0.204D$. (F) The contour map of $\sigma_y(D, l)$ in (A). The ridge is fitted by $l^* = 0.21(D^* - 50)^{0.62} + 1$ (dashed curve).

σ_y, which is sufficient to average out most noises [36]. The measured $\sigma_y(D, l)$ are shown in Figures 2B, 3A, 3B.

$\sigma_y(D)$ in Figure 2B increases and reaches a plateau at $l = 1$ and monotonically increases at $l > 1$. Both the plateau and increases are considered as the IHP behavior [17] as they deviate from the HP behavior of the monotonic decrease of $\sigma_y(D)$. By contrast, 3D polycrystals exhibit both the HP and IHP behaviors [17]. Studies on $\sigma_y(D)$ in 2D are very limited and focus only on polycrystals with norm thin GBs (i.e., $l = 1$) [23, 24]. These studies only observed the IHP behavior without HP behavior, which has been attributed to the lack of dislocations in 2D [37]. A perfect 2D crystal lacks a source to generate dislocations according to the dislocation pile-up model [38]. Dislocations in 2D crystals are point defects that cannot entangle and can thus be easily absorbed by GBs. By contrast, dislocations in 3D crystals are topological line defects that

can entangle into complex structures and cannot be easily absorbed by GBs. Thus, the HP behavior caused by dislocation motions is often absent in 2D polycrystals with normal thin GBs [23, 24]. Thick GBs further suppress dislocations and their motions, thus the HP behavior is absent in Figure 2B.

As shown in Figure 3A, $\sigma_y(l)$ monotonically decreases at $D < 50$, and changes non-monotonically with a peak at $D > 50$. They can be fitted by $\sigma_y(D,l) = e^{a_1 - l/a_2} - a_3 l^{-1} + 44$. The constant 44 is the yield stress directly measured from the completely amorphous sample. l^{-1} term has been predicted by ref. [39] as the effect of thick grain boundaries with strain gradient. The fittings in Figures 3C–3E further show $\sigma_y(D,l) = 0.17D^{0.35}e^{-\frac{l}{0.08D+1.34}} - 0.204D/l + 44$, and the competition between the exponential term and D/l term gives the peak of σ_y. The strength peak σ_y^* corresponds to D^* and l^*, which can be fitted by a power law $D^*(l^*)$, as shown by the dashed curve in Figure 3F. Since D^*/l^* is not a constant, σ_y^* is not solely determined by A_{GB}/A_{tot}. In addition, σ_y^* should exhibit a maximum rather than the monotonic increase with D^* and l^* in Figure 3F, but it is beyond the system size of our simulation. For normal polycrystals with $l = 1$, the fitted $D^* = 50$ in Figure 3F for our 2D crystals is analogous to the peak position at the HP-IHP boundary of 15 nm (i.e., about 100 atoms) for typical 3D polycrystals. Interestingly, when σ_y at fixed D is plotted as a function of the area fraction of GB, A_{GB}/A_{tot}, all curves collapse at $A_{GB}/A_{tot} > 20\%$ (Figure 3B). This indicates that σ_y is dictated by the total fraction of amorphous or crystalline regions, but is not sensitive to their spatial distribution. When $A_{GB}/A_{tot} > 50\%$, σ_y equals to that of the completely disordered glass, i.e., the crystalline regions do not affect σ_y. When $A_{GB}/A_{tot} < 20\%$, larger grains yield at larger σ_y. The simulation in ref. [40] reports that σ_y increases with the fraction of crystalline regions, i.e., decreases with A_{GB}/A_{tot} as shown in most regimes in Figure 3B. Nevertheless, ref. [40] measures only one curve without fixing D or l, thus are not related to the generalization of the HP and IHP behaviors.

DEFORMATION MECHANISMS

For large-grain ($D \geqslant 50$) samples with $l \leqslant 10$, GBs emit dislocations that glide through one grain and are absorbed by nearby GBs, see the yellow line segments in Figure 4A. Note that dislocations in small 2D crystalline grains can be easily absorbed by GBs, thus they only temporarily exist when they glide through the grains. Such dislocation motion is the major mode of plastic deformation. We observe that dislocations

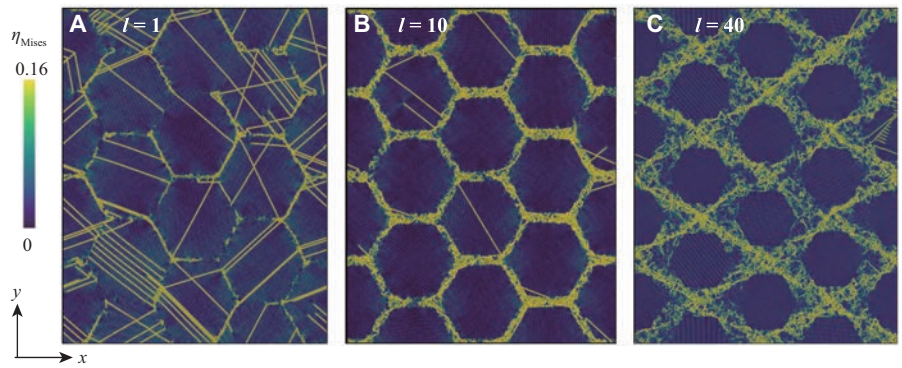

Figure 4 von Mises shear strain η_{Mises} of $D = 100$ samples with different GB thicknesses under $\varepsilon = 5.0\%$. (A) At $l = 1$, many dislocations glide through crystalline grains (yellow lines). (B) At $l = 10$, most plastic deformations occur in GBs. (C) At $l = 40$, almost all the plastic deformations occur in GBs.

are more difficult to be emitted and easily absorbed by thicker GBs, in accordance with previous studies on Cu-Zr GCCs [8, 13]. As l increases, the dislocation motions give way to another mode of deformation, namely, GB deformations (Figures 4B and 4C). Thick GBs suppress dislocations but promote GB sliding. These two opposite effects on plastic deformation result in a peak of $\sigma_y(l)$ at $l = 3$ for the samples with $D = 100$ (Figure 4D). When $l > 10$ and $D = 100$ (i.e., $A_{GB}/A_{tot} > 20\%$), all the applied plastic deformation is borne by the GB sliding in amorphous regions. Therefore, σ_y is solely determined by A_{GB}/A_{tot} and insensitive to D, which explains the collapsed σ_y at $A_{GB}/A_{tot} > 20\%$ shown in Figure 3B. Similarly, dislocations barely exist in small crystalline grains, and thus all the applied plastic deformation is borne within the amorphous regions for samples with $D < 50$ (Figure S2). Therefore, $\sigma_y(l)$ monotonically decreases at $D < 50$.

Deformations are dominated by dislocation motions in crystalline regions [41] and by GB sliding [42,43], GB diffusion creep [44, 45] and shear banding in amorphous regions. These basic modes of deformation widely exist in polycrystals, glasses and their hybrid structures [41]. They have been used to explain the HP and IHP behaviors of $\sigma_y(D)$ in normal polycrystals with $l = 1$. Here, we similarly use these modes to explain the generalized HP- and IHP-like behaviors in $\sigma_y(D, l)$. As D varies, the competition between the deformations via dislocations and GBs gives rise to the classical HP and IHP behaviors with a peak of σ_y at $D \simeq 15$ nm for most 3D polycrystals. Such a competition of the two modes of deformations shown in Figure 4 similarly gives rise to a peak of $\sigma_y(l)$ when $D \geqslant 50$ in Figure 3A because reducing D has a similar effect to increasing l, i.e., increasing the fraction of amorphous regions. The increasing and decreasing part of $\sigma_y(l)$ at a fixed D are analogous to the classical HP and IHP behaviors of $\sigma_y(D)$, respectively, at a fixed $l = 1$.

The fraction of large-strain ($\eta_{Mises} > 16\%$) particles in GBs changes monotonically with ε (Figures 5A and S4) as expected, but non-monotonically with l, as shown in Figure 5B. For example, the fractions at different ε all reach maxima at $l = 10$ in samples with $D = 100$, as shown in Figure 5B. The peaks in Figures 5B and 5C divide $\sigma_y(l)$ into three regimes, see Figure 5C as an example at $D = 100$.

Besides the shear strains of individual particles in Figure 4, the relative motions between particles are characterized using (1) a reference line (Figures 6A–6F, S5, S6); and (2) a displacement field (Figures 6G–6I). A row of particles is chosen as a reference line to highlight the key parts of the deformation. It has been used in simulation [46] and colloid experiment [47], but rarely in atomic polycrystals because atomic motions can hardly be tracked under electron microscopy. In Figures 6G–6I, the displacement vectors are obtained by linking the initial position to the final position of the particles after subtracting the background

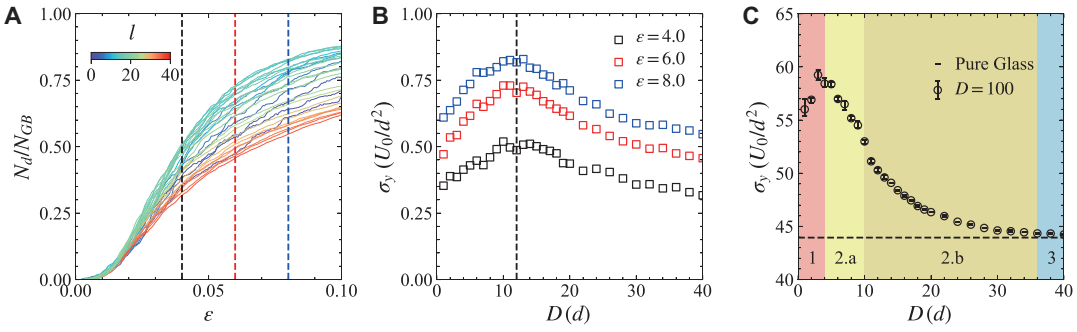

Figure 5 Deformation of GCCs with $D = 100$ and different l. (A), (B) Fraction of particles with large deformation ($\eta_{Mises} > 0.16$) on GBs (A) increases with ε and (B) changes non-monotonically with l. The three curves in (B), corresponding to the values on the three vertical dashed lines in (A), all reach the maxima at $l = 10$. (C) $\sigma_y(l)$ is divided into three regimes.

affine deformation. Such vector field shows both the magnitude and direction of particles' displacements relative to the background; thus, it can better illustrate the collective motions. The reference line has been used to illustrate the shear-coupled GB migration [46, 47] and the displacement field has often been used in fluid flows. Figures 6D and 6E show that the compression along the x direction deforms the initially straight yellow reference line into small steps. Each step is along the [01] lattice directions inside the grains and random directions in GBs, see ellipses in Figure 6E. A newly formed step inside a crystalline region is caused by a dislocation gliding through the reference line. A gliding dislocation produces a straight line in the displacement field, as shown in Figure 6D. Deformations are mainly due to the dislocation sliding at $l < 10$ and GB sliding at $l \geqslant 10$ (Figure 6). At $l \geqslant 10$, the bending of the reference line is localized to one large step near the middle of two triple junctions (ellipse in Figure 6F), that is, the center of a swirl (Figure 6I). Particles with large displacements are near the triple junctions (Figures 6E and 6F). The compression along the x direction expands l to l_2 for GBs along the x direction and reduces l to l_1 for GBs along ±120° directions (Figure 6E) because the amorphous regions have a positive Poisson ratio. The total amorphous area remains the same.

Interestingly, the displacement field in each crystalline grain exhibits a flower shape with a bright center, that is, a region with zero displacements (Figure 7B). The two-in-two-out flow field (blue arrows in Figure 7C) around each fixed point (i.e., bright spot) demonstrates that the bright spot is a topological defect with charge –1 commonly observed in liquid crystals [48]. Such flow pattern reflects the compression and elongation along the x and y directions, respectively. A "flower" has more than four bright "petals" because there are more directions for vectors to be parallel, and thus they strongly overlap and produce brighter regions (Figure

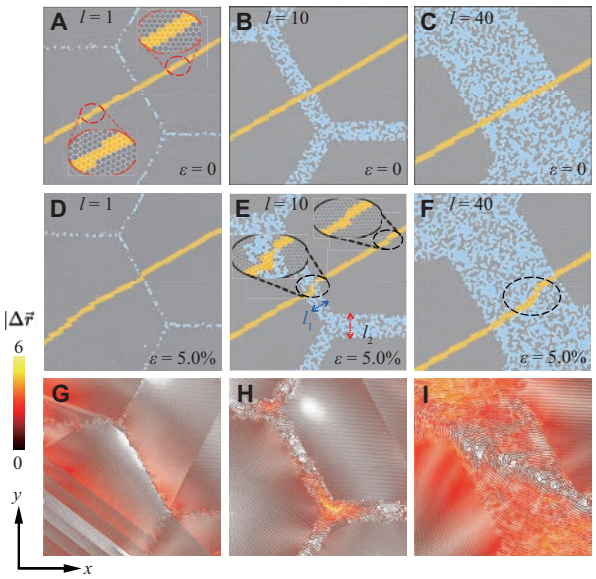

Figure 6 The GCCs with $D = 100$ and ((A), (D), (G)) $l = 1$; ((B), (E), (H)) $l = 10$; ((C), (F), (I)) $l = 40$ under the uniaxial compression along the x direction. GBs are composed of small (grey) and large (blue) particles. (A)–(C) Three rows of particles labeled in yellow serve as the initial reference line at $\varepsilon = 0$. The three neighboring rows in each image makes the yellow line thick enough to be easily seen. The yellow line is along the [11] lattice direction for the right grain, but not for the left grain; thus, several small steps are in the initial straight yellow line. (D)–(F) Deforming (A)–(C) by $\varepsilon = 5.0\%$. Different GBs are deformed into different thicknesses l_1 and l_2. (G)–(I) The fields of particles displacement vectors $\Delta\vec{r}$ at $\varepsilon = 5.0\%$, which correspond to (D)–(F), respectively. $|\Delta\vec{r}|$ can also be seen from the colors.

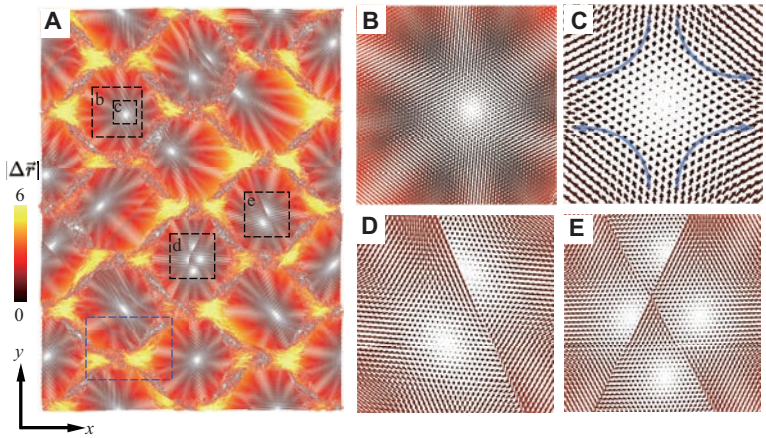

Figure 7 Displacement field for the sample with $(D, l) = (100, 40)$ under $\varepsilon = 7.5\%$. (A) Each grain has a flower-like pattern. (B)–(E) The zoom-in subareas are labeled in (A). (B), (C) The center of a flower is a fixed point with a topological charge of –1. (D) A flower is cut by a dislocation gliding (straight line, i.e., a domain wall), forming topological charges –1 and –1/2. (E) A flower is cut by two dislocation gliding, forming two –1 charges and two –1/2 charges with two domain walls.

7B). Usually, a flower has six or twelve bright petals, which reflect the six-fold symmetry of the hexagonal lattice. As a topological defect, a dislocation glides through a flower and cuts it into two topological defects with a domain wall (Figures 7D and 7E).

CONCLUSION AND DISCUSSION

We systemically measured the properties of the 2D GCCs with different GB thicknesses l and mean grain diameters D. The classical HP and IHP behaviors of strength $\sigma_y(D)$ at $l = 1$ are generalized for the first time in two directions: (1) $\sigma_y(D)$ at $l > 1$ (Figure 2B) and (2) $\sigma_y(l)$ at a fixed D (Figure 3A). For direction (1), only IHP behavior is observed, in accordance with the absent HP behavior reported in 2D polycrystalline graphene [23, 24] and silicene [25]. The absent HP behavior is attributed to the lack of dislocations because they cannot entangle in 2D and thus can be easily absorbed into GBs. For direction (2), $\sigma_y(l)$ exhibits a peak at $l^*(D)$ when $D \geqslant 50$ due to the competition between the deformations via dislocations and GBs (Figure 4), and monotonically decreases when $D < 50$ because GB deformations dominate (Figure S2). The increases and decreases of $\sigma_y(l)$ in Figure 3A are analogous to the classical HP and IHP behaviors of $\sigma_y(D)$, respectively, because both increasing l and decreasing D increase the amorphous fraction $A_{\mathrm{GB}}/A_{\mathrm{tot}}$. As $A_{\mathrm{GB}}/A_{\mathrm{tot}}$ increases, dislocation gliding gradually gives way to GB sliding or deformation inside GBs, that is, the mechanism of HP behavior giving way to the mechanism of IHP behavior as D decreases in normal 3D polycrystals. Therefore, the general HP and IHP behaviors in $\sigma_y(D, l)$ can be unified as $\sigma_y(A_{\mathrm{GB}}/A_{\mathrm{tot}})$, as shown in the collapse in Figure 3B. Although simulations for large (D, l) in 3D are challenging, our generalization of HP and IHP behaviors of $\sigma_y(D, l)$ in 2D could similarly exist in 3D because the competition between dislocation motion and GB deformation similarly exists in both 2D and 3D. Furthermore, the HP regimes due to dislocation motions should be wider in 3D compared with those in 2D because 3D solids have much more dislocations. Another prediction is that the HP behavior of $\sigma_y(D)$ should be absent in 3D at large l because the thick GBs, also known as the amorphous intergranular films in 3D [13], suppress the dislocation

motions. It is worth noting that the deformation mechanism in real materials can be more complicated, such as caused by residual stress from the fabrication process [49] or via cracking in brittle materials [50], which may affect the HP and IHP behaviors. Moreover, the grain sizes are not uniform in real materials which may produce less sharp peak of $\sigma_y(D, l)$ in Figure 3 due to the mixed deformation mechanisms of thin and thick GBs.

The traditional $\sigma_y(D)$ classifies normal polycrystals with $l = 1$ into three regimes: the HP regime ($D \gtrsim 15$ nm), the IHP regime (3 nm $\lesssim D \lesssim$ 15 nm), and unstable regime ($D \lesssim 3$ nm) up to the amorphous limit $D = 0$. As an analogy, we classify solids into three regimes using $\sigma_y(l)$ at a fixed D, see the example at $D = 100$ in Figure 5C: (1) the HP-like regime at $l \leqslant 3$; (2) the IHP-like regime which can be further divided by the peak in Figure 5B as (2a) the competition between dislocation motion and GB sliding ($3 < l < 10$) and (2b) only GB sliding ($10 < l < 40$, i.e. $20\% < \sigma_y(A_{\rm GB}/A_{\rm tot}) < 50\%$); and (3) the glass regime. In regime (2b), σ_y only depends on the total fraction of amorphous region, not depends on grain size distribution, see the collapse in Figure 3B. In regime (3), $\sigma_y(l)$ is independent to the crystalline regions at $l > 40$, i.e., $\sigma_y(A_{\rm GB}/A_{\rm tot}) > 50\%$ (Figures 3A and 3B). The dislocation gliding mechanism in HP-like regimes and the GB deformation mechanism in IHP-like regimes are observed by strain fields (Figure 4), deformation steps on a reference line (Figures 6A–6C), and displacement vector fields (Figures 6D–6F). Steps in the reference line are along the lattice direction due to dislocation gliding in the crystalline regions, but localized at the center of the swirl in each thick GB. Particles in triple junctions have the maximum displacements. Particles' displacements in each crystalline grain exhibit a two-in-two-out flow around a fixed point, that is, a topological charge of –1 commonly observed in liquid crystals. A dislocation gliding through the field can cut the topological charge into two.

To the best of our knowledge, HP and IHP behaviors have only been generalized by tuning the twin-boundary spacing inside grains of polycrystal in simulation [36]. In the current study, our generalizations along the other two directions bridge the crystal and amorphous solids beyond polycrystals. As a by-product of the generalization, both ref. [36] and our results provide ways to exceed the conventional maximum strength of $\sigma_y(D)$ by tuning new parameters. Which microstructure gives the maximum strength is an important question. The strength of normal polycrystals reaches the maximum at $l \simeq 15$ nm, that is, the boundary between the HP and IHP regimes. Here, we show that expanding GBs can further enhance the strength and reach the maximum at $l^*(D)$, as shown in Figure 3C. Besides strength, the ductility, fatigue life and other material properties can be similarly studied as a function of (D, l) in this system, which can guide the fabrication of high-strength materials. This system can also be used to study the polycrystal-glass transformation via a new approach by changing l, in contrast to changing D in ref. [51]. These results are of basic importance in materials science and have practical implications for GCC and super alloy fabrications.

Data availability

Data that support the plots within this paper are available from the corresponding authors upon reasonable request. Source data and simulation code are available for this paper.

Acknowledgements

We thank Rui Zhang, Yang Xiang, Qingping Sun, Xian Chen, Peng Hua, Wei Li, and Kaiyao Qiao for insightful discussion.

Funding

This work was supported by the Guangdong Basic and Applied Basic Research Foundation (2020B1515120067), the Hong Kong Research Grants Council under the Collaborative Research Fund (CRF-C6016-20G and CRF-C6021-19EF), the Fundamental Research Funds for the Central Universities (xxj032021001), the Key R&D Project of Shaanxi Province (2022GY-400) and the National Natural Science Foundation of China (12274336).

Author contributions

Y.H. conceived the idea. Z.X. performed the simulation and analyzed the data with the help of M.L., H.Z., and Y.H. Y.H. and Z.X. proposed the analysis methods and interpreted the data. Z.X. and Y.H. wrote the manuscript. Y.H. supervised the project. All authors discussed the results.

Conflict of interest

The authors declare no conflict of interest.

Supplementary information

The supporting information is available online at https://doi.org/10.1360/nso/20220058. The supporting materials are published as submitted, without typesetting or editing. The responsibility for scientific accuracy and content remains entirely with the authors.

References

1 Greer AL. Metallic glasses. *Science* 1995; **267**: 1947–1953.
2 Ma Y, Yang M, Yuan F, *et al*. A review on heterogeneous nanostructures: A strategy for superior mechanical properties in metals. *Metals* 2019; **9**: 598.
3 Deb SK, Wilding M, Somayazulu M, *et al*. Pressure-induced amorphization and an amorphous-amorphous transition in densified porous silicon. *Nature* 2001; **414**: 528–530.
4 Mishima O, Calvert LD, Whalley E. "Melting ice" I at 77 K and 10 kbar: a new method of making amorphous solids. *Nature* 1984; **310**: 393–395.
5 Li FC, Liu T, Zhang JY, *et al*. Amorphous-nanocrystalline alloys: fabrication, properties, and applications. *Mater Today Adv* 2019; **4**: 100027.
6 Wu G, Chan KC, Zhu L, *et al*. Dual-phase nanostructuring as a route to high-strength magnesium alloys. *Nature* 2017; **545**: 80–83.
7 Su R, Neffati D, Cho J, *et al*. High-strength nanocrystalline intermetallics with room temperature deformability enabled by nanometer thick grain boundaries. *Sci Adv* 2021; **7**: eabc8288.
8 Wang Y, Li J, Hamza AV, *et al*. Ductile crystalline-amorphous nanolaminates. *Proc Natl Acad Sci USA* 2007; **104**: 11155–11160.
9 Hua P, Xia M, Onuki Y, *et al*. Nanocomposite NiTi shape memory alloy with high strength and fatigue resistance. *Nat Nanotechnol* 2021; **16**: 409–413.
10 Li F, Zhao H, Yue Y, *et al*. Dual-phase super-strong and elastic ceramic. *ACS Nano* 2019; **13**: 4191–4198.
11 He B, Hu B, Yen H, *et al*. High dislocation densit-induced large ductility in deformed and partitioned steels. *Science* 2017; **357**: 1029–1032.
12 Hua P, Chu K, Sun Q. Grain refinement and amorphization in nanocrystalline NiTi micropillars under uniaxial compression. *Scrip Mater* 2018; **154**: 123–126.
13 Pan Z, Rupert TJ. Amorphous intergranular films as toughening structural features. *Acta Mater* 2015; **89**: 205–214.
14 Xiao J, Deng C. Mitigating the Hall-Petch breakdown in nanotwinned Cu by amorphous intergranular films. *Scripta Mater* 2021; **194**: 113682.

15 Neelav AH, Pal S, Deng C. Atomistic investigation of the deformation mechanisms in nanocrystalline Cu with amorphous intergranular films. *J Appl Phys* 2019; **126**: 125101.

16 Li RN, Song HY, An MR, *et al*. Atomic-scale insight into mechanical properties and deformation behavior of crystalline/amorphous dual-phase high entropy alloys. *Phys Lett A* 2022; **446**: 128272.

17 Naik SN, Walley SM. The Hall-Petch and inverse Hall-Petch relations and the hardness of nanocrystalline metals. *J Mater Sci* 2020; **55**: 2661–2681.

18 Hall EO. The deformation and ageing of mild steel: III discussion of results. *Proc Phys Soc B* 1951; **64**: 747–753.

19 Petch N. The cleavage strength of polycrystals. *J Iron Steel Inst* 1953; **174**: 25-28.

20 Chokshi AH, Rosen A, Karch J, *et al*. On the validity of the Hall-Petch relationship in nanocrystalline materials. *Scripta Metall* 1989; **23**: 1679–1683.

21 Schiøtz J, Jacobsen KW. A maximum in the strength of nanocrystalline copper. *Science* 2003; **301**: 1357–1359.

22 Trelewicz JR, Schuh CA. The Hall-Petch breakdown in nanocrystalline metals: A crossover to glass-like deformation. *Acta Mater* 2007; **55**: 5948–5958.

23 Song Z, Artyukhov VI, Yakobson BI, *et al*. Pseudo Hall-Petch strength reduction in polycrystalline graphene. *Nano Lett* 2013; **13**: 1829–1833.

24 Han J. The transition from an inverse pseudo Hall-Petch to a pseudo Hall-Petch behavior in nanocrystalline graphene. *Carbon* 2020; **161**: 542–549.

25 Rakib T, Saha S, Motalab M, *et al*. Atomistic representation of anomalies in the failure behaviour of nanocrystalline silicene. *Sci Rep* 2017; **7**: 14629.

26 Liu J, Ji Y, Nai J, *et al*. Ultrathin amorphous cobalt-vanadium hydr(oxy)oxide catalysts for the oxygen evolution reaction. *Energy Environ Sci* 2018; **11**: 1736–1741.

27 Wang X, Li Y, Wang S, *et al*. 2D amorphous V_2O_5/graphene heterostructures for high-safety aqueous Zn-Ion batteries with unprecedented capacity and ultrahigh rate capability. *Adv Energy Mater* 2020; **10**: 2000081.

28 Zhao H, Chen X, Wang G, *et al*. Two-dimensional amorphous nanomaterials: synthesis and applications. *2D Mater* 2019; **6**: 032002.

29 Ding J, Neffati D, Li Q, *et al*. Thick grain boundary induced strengthening in nanocrystalline Ni alloy. *Nanoscale* 2019; **11**: 23449–23458.

30 Plimpton S. Fast parallel algorithms for short-range molecular dynamics. *J Comput Phys* 1995; **117**: 1–19.

31 Nie Y, Liu J, Guo J, *et al*. Connecting glass-forming ability of binary mixtures of soft particles to equilibrium melting temperatures. *Nat Commun* 2020; **11**: 3198.

32 Pedersen UR, Schrøder TB, Dyre JC. Phase diagram of Kob-Andersen-type binary Lennard-Jones mixtures. *Phys Rev Lett* 2018; **120**: 165501.

33 Tsai DH. The virial theorem and stress calculation in molecular dynamics. *J Chem Phys* 1979; **70**: 1375–1382.

34 Zhou M. A new look at the atomic level virial stress: on continuum-molecular system equivalence. *Proc R Soc Lond A* 2003; **459**: 2347–2392.

35 Pastor-Abia L, Caturla MJ, SanFabián E, *et al*. Stress-strain curves of aluminum nanowires: Fluctuations in the plastic regime and absence of hardening. *Phys Rev B* 2008; **78**: 153410.

36 Li X, Wei Y, Lu L, *et al*. Dislocation nucleation governed softening and maximum strength in nano-twinned metals. *Nature* 2010; **464**: 877–880.

37 Zhu Y, Wang H, Zhu X, *et al*. A continuum model for dislocation dynamics incorporating Frank-Read sources and Hall-Petch relation in two dimensions. *Int J Plast* 2014; **60**: 19–39.

38 Pande CS, Masumura RA, Armstrong RW. Pile-up based hall-petch relation for nanoscale materials. *Nanostructured Mater* 1993; **2**: 323–331.

39 Zhang X, Aifantis KE. Interpreting the softening of nanomaterials through gradient plasticity. *J Mater Res* 2011; **26**: 1399–1405.

40 Brink T, Albe K. From metallic glasses to nanocrystals: Molecular dynamics simulations on the crossover from glass-like to grain-boundary-mediated deformation behaviour. *Acta Mater* 2018; **156**: 205–214.

41 Li X, Wei Y, Yang W, *et al*. Competing grain-boundary- and dislocation-mediated mechanisms in plastic strain recovery in nanocrystalline aluminum. *Proc Natl Acad Sci USA* 2009; **106**: 16108–16113.

42 Guo D, Song S, Luo R, *et al*. Grain boundary sliding and amorphization are responsible for the reverse Hall-Petch relation in superhard nanocrystalline boron carbide. *Phys Rev Lett* 2018; **121**: 145504.

43 Quek SS, Chooi ZH, Wu Z, *et al*. The inverse Hall-Petch relation in nanocrystalline metals: A discrete dislocation dynamics analysis. *J Mech Phys Solids* 2016; **88**: 252–266.

44 Wei Y, Bower AF, Gao H. Recoverable creep deformation and transient local stress concentration due to heterogeneous grain-boundary diffusion and sliding in polycrystalline solids. *J Mech Phys Solids* 2008; **56**: 1460–1483.

45 Ford JM, Wheeler J, Movchan AB. Computer simulation of grain-boundary diffusion creep. *Acta Mater* 2002; **50**: 3941–3955.

46 Thomas S, Chen K, Han J, et al. Reconciling grain growth and shear-coupled grain boundary migration. *Nat Commun* 2017; **8**: 1764.

47 Li W, Peng Y, Zhang Y, *et al*. Shear-assisted grain coarsening in colloidal polycrystals. *Proc Natl Acad Sci USA* 2020; **117**: 24055–24060.

48 Chaikin P, Lubensky T, Witten T. *Principles of Condensed Matter Physics*. Cambridge: Cambridge University Press, 1995

49 Withers PJ, Bhadeshia HKDH. Residual stress. Part 1—Measurement techniques. *Mater Sci Tech* 2001; **17**: 355–365.

50 Li F, Liu T, Wang T, *et al*. Understanding yielding and the unusual ductile-brittle-ductile transition in Fe-based amorphous nanocrystalline alloy: A combined micromechanical and thermodynamic study. *J Mech Phys Solids* 2019; **132**: 103681.

51 Zhang H, Han Y. Compression-induced polycrystal-glass transition in binary crystals. *Phys Rev X* 2018; **8**: 041023.